Effects of Self-Assembled Monolayers on Solid-State CdS Quantum Dot Sensitized Solar Cells

Pendar Ardalan,[†] Thomas P. Brennan,[†] Han-Bo-Ram Lee,[†] Jonathan R. Bakke,[†] I-Kang Ding,[‡] Michael D. McGehee,[‡] and Stacey F. Bent[†,*]

[†]Department of Chemical Engineering and [‡]Department of Materials Science and Engineering, Stanford University, Stanford, California 94305, United States

ABSTRACT Quantum dot sensitized solar cells (QDSSCs) are of interest for solar energy conversion because of their tunable band gap and promise of stable, low-cost performance. We have investigated the effects of self-assembled monolayers (SAMs) with phosphonic acid headgroups on the bonding and performance of cadmium sulfide (CdS) solid-state QDSSCs. CdS quantum dots ~2 to ~6 nm in diameter were grown on SAM-passivated planar or nanostructured TiO_2 surfaces by successive ionic layer adsorption and reaction (SILAR), and photovoltaic devices were fabricated with spiro-OMeTAD as the solid-state hole conductor. X-ray photoelectron spectroscopy, Auger electron spectroscopy, ultraviolet−visible spectroscopy, scanning electron microscopy, transmission electron microscopy, water contact angle measurements, ellipsometry, and electrical measurements were employed to characterize the materials and the resulting device performance. The data indicate that the nature of the SAM tailgroup does not significantly affect the uptake of CdS quantum dots on TiO_2 nor their optical properties, but the presence of the SAM does have a significant effect on the photovoltaic device performance. Interestingly, we observe up to ~3 times higher power conversion efficiencies in devices with a SAM compared to those without the SAM.

KEYWORDS: quantum dot sensitized solar cells · self-assembled monolayers · successive ionic layer adsorption and reaction · cadmium sulfide · titanium dioxide · nanostructure

On the basis of the ever-increasing demand for clean energy, environmentally sustainable energy resources need to be investigated. Here, the major problem to tackle is coming up with energy resources capable of producing ~23 TW of carbon-emission-free power by 2050.[1] Among various options such as geothermal, wind power, and solar energy, exploitation of solar radiation stands out to be the most viable choice mainly due to the fact that no other energy supply is more plentiful than the 120 000 TW the sun provides.[1,2] However, to achieve the aforementioned goals, new efforts should be made to fabricate low-cost photovoltaic devices that can harvest the photons more efficiently.[1,2]

Dye-sensitized solar cells (DSSCs) are one attractive class of low-cost photovoltaics with alternative structures to that of conventional solar cells. At the heart of a DSSC is a monolayer of charge transfer dye which is attached to a mesoporous oxide layer (typically anatase titanium dioxide (TiO_2)).[3,4] Power conversion efficiencies of ~11% have been reported using such structures.[3,5] On the other hand, narrow band gap nanostructures such as CdS quantum dots (QDs) are known to show stability and size quantization effects as well as the possibility of multiple exciton generation (MEG) from a single incident photon.[6,7] They are therefore beneficial for absorption of light in the visible and near-infrared region of the solar spectrum and can be used to fabricate photovoltaic devices with high theoretical efficiencies.[8] In quantum dot sensitized solar cells (QDSSCs), the QDs can be engineered to transfer the electron to a wide band gap semiconductor such as TiO_2 or zinc oxide (ZnO).[8]

In both DSSCs and QDSSCs, it is desirable that the liquid electrolyte in traditional cell designs be replaced with a solid-state hole conductor to avoid sealing and ameliorate long-term stability problems.[9,10] However, performance in such devices is reduced by electron−hole recombination at the TiO_2−hole conductor interface,[11] which is faster than the analogous process in liquid electrolyte devices.[9] Hence, the use of passivation layers[12] and organic linkers such as self-assembled monolayers (SAMs)[13] on these devices could provide a means of eliminating recombination sites and lead to increased efficiency.[11] In the case of QDSSCs, SAMs also enhance the CdS QDs' linkage to TiO_2.[14]

It has been reported that SAMs with phosphonic acid headgroups provide the strongest attachment to TiO_2.[15,16] Hence, in this study, we have employed various spectroscopic techniques to investigate the effects of a SAM with a phosphonic acid headgroup and varied tailgroups (Figure 1) on the bonding of CdS QDs on both planar

* Address correspondence to sbent@stanford.edu.

Received for review December 8, 2010 and accepted January 21, 2011.

Published online February 07, 2011
10.1021/nn103371v

and nanostructured TiO_2 surfaces as well as on the performance of CdS solid-state QDSSCs.

In this work, we demonstrate control over the average size of the CdS QDs by employing a solution-based growth technique known as successive ionic layer adsorption and reaction (SILAR).[17] SILAR is suitable for growing thin films of water-insoluble, ionic compounds from solution on a solid substrate,[17] and it has been shown that QDs can be grown with only a few SILAR cycles.[11,18,19] Moreover, we show that although no significant change in CdS uptake on mesoporous TiO_2 surfaces is observed when a SAM layer is employed, the presence of the SAM layer results in approximately a 3-fold increase in maximum power conversion efficiency in the devices. We suggest that this effect is related to the presence of a SAM-based electron−hole recombination barrier or passivation layer. The results have implications for the design of improved QDSSCs.

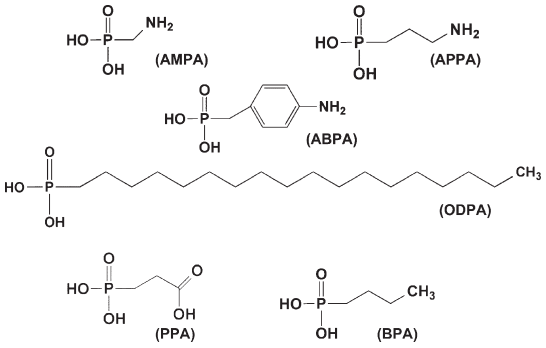

Figure 1. Schematic view of the phosphonic acid SAMs studied in the current work: the amine-terminated molecules aminomethylphosphonic acid (AMPA), 3-aminopropylphosphonic acid (APPA), and 4-aminobenzylphosphonic acid (ABPA), the methyl-terminated molecules 1-butylphosphonic acid (BPA) and *n*-octadecylphosphonic acid (ODPA), and the carboxylic acid-terminated molecule 3-phosphonopropionic acid (PPA).

RESULTS AND DISCUSSION

SAM Growth and CdS Uptake on Planar Surfaces. Figure 2 shows X-ray photoelectron spectroscopy (XPS) survey scans of the Si/SiO_2 surface after TiO_2 atomic layer deposition (ALD), after APPA SAM growth, and after 3 and 10 CdS SILAR cycles. Figure 3a,b shows high-resolution XP spectra of Cd(3d) and S(2s) taken after 10 SILAR cycles were completed at the APPA-coated planar surface, respectively. In addition to the spectra shown, a high-resolution Ti(2p) scan indicates that, after TiO_2 ALD, spin−orbit split $Ti(2p_{3/2})$ and $Ti(2p_{1/2})$ peaks are observable at 458.4 and 464.1 eV, respectively, which agrees well with the reported values for TiO_2.[20−23]

After the APPA SAM growth, N and P are detected at the surface (similar results are observed in the Auger electron spectra of the APPA-coated surface, Supporting Information Figure S1). Moreover, the water contact

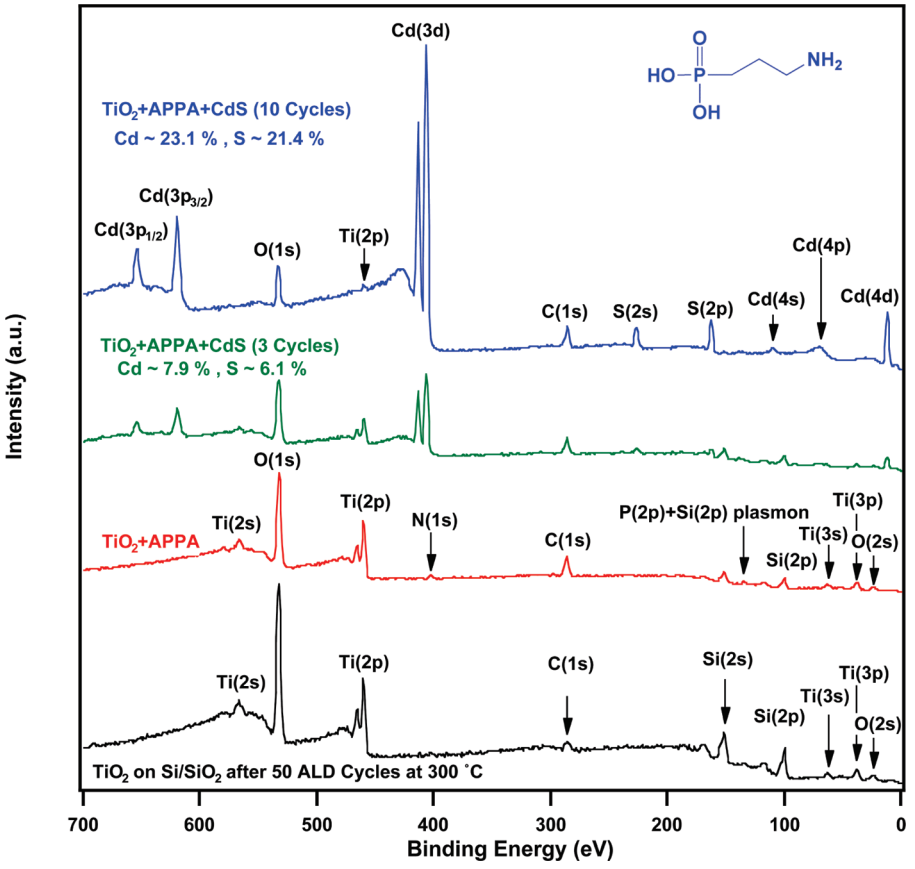

Figure 2. XP spectra of Si/SiO_2 surface after 50 cycles of TiO_2 ALD, APPA SAM growth, 3 and 10 CdS SILAR cycles. All spectra are shown on the same scale.

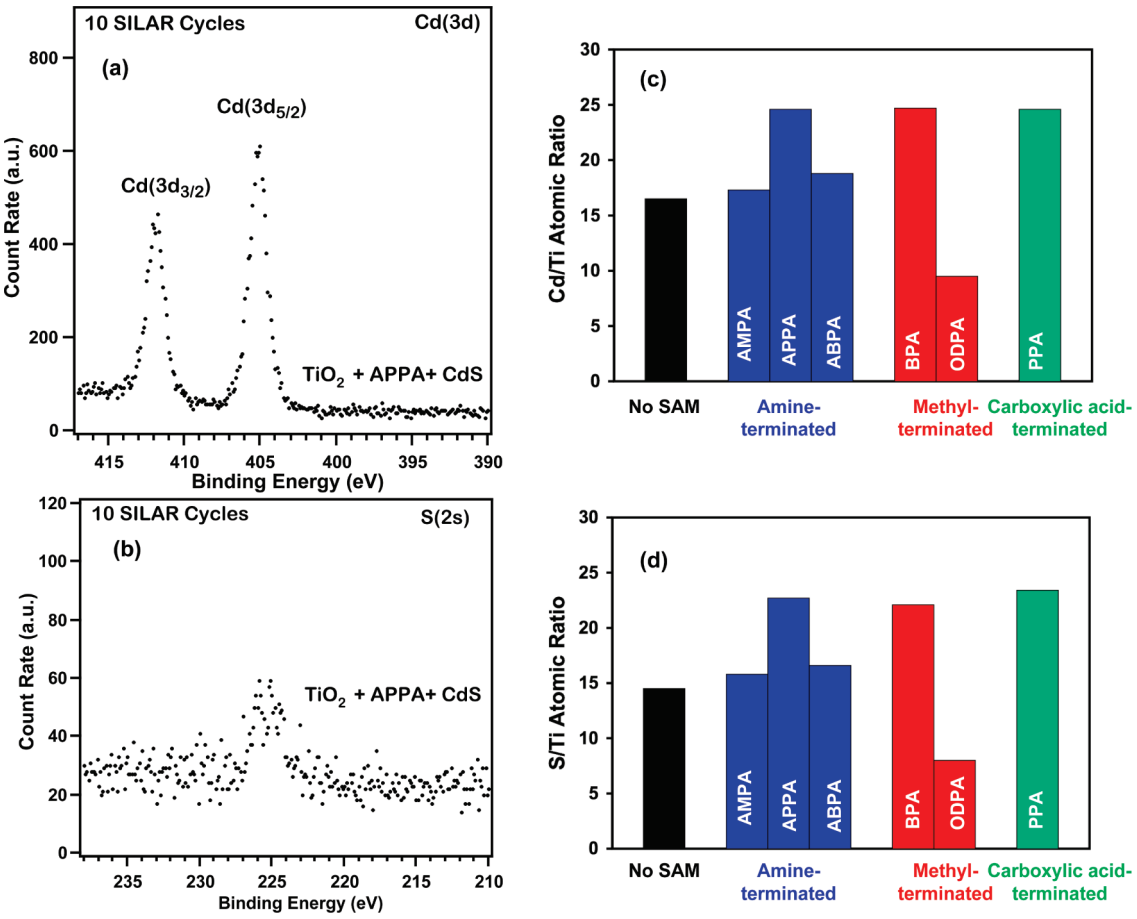

Figure 3. High-resolution XP spectra of (a) Cd(3d) and (b) S(2s) taken after 10 CdS SILAR cycles. (c) Cd to Ti atomic ratio and (d) S to Ti atomic ratio values calculated from the XP survey scans for the SAM-coated planar TiO_2 surfaces and the surface with no SAM.

angle (WCA) value corresponding to the APPA SAM is 38.6 ± 1.8°. In transmission IR studies, we have investigated the peak position and broadening of the methylene (CH_2) stretching modes (indicative of conformational ordering in the SAM alkyl chains). Those IR spectra show peaks similar to those reported for liquid-like alkanes in the literature (Supporting Information Figure S2).[24,25] This result together with the low value of the WCA suggests the presence of a hydrophilic and disordered SAM with a low degree of packing at the surface. Similar results were observed for the other SAMs with a short alkyl chain regardless of the nature of the tailgroup (*i.e.*, AMPA, BPA, and PPA) as well as the aromatic SAM (ABPA). However, for the long-chain methyl-terminated SAM (ODPA), the WCA (104.8 ± 1.9°) and film thickness (12.5 ± 0.8 Å) values along with the position of the methylene (CH_2) stretching modes (2920 and 2850 cm^{-1}) indicate the presence of a well-packed monolayer with midrange ordering (Supporting Information Figure S2).[24,25]

After CdS SILAR, the binding energies of the Cd(3d) peaks as well as the S(2s) peak (Figure 3a,b) are in agreement with the presence of CdS.[26] Moreover, elemental composition analysis based on XPS survey scans shows that CdS is near stoichiometric. Similar XPS results were observed after CdS SILAR at the surface of the other SAMs studied in this work as well as at the control surface without a SAM. Auger electron spectra of the APPA-coated surface after 3, 6, and 10 CdS SILAR cycles presented in the Supporting Information (Figure S1) confirm the XPS results. Cd/Ti and S/Ti atomic ratios, which are calculated by analyzing the XPS survey scans, are also shown in Figures 3c,d for each of the substrates studied after 10 SILAR cycles. At planar surfaces, somewhat higher CdS amounts are detected after 10 SILAR cycles on each sample containing a SAM compared to the sample without a SAM, with the exception of the long-chain methyl-terminated SAM (ODPA). The lower CdS deposition on ODPA is attributed to the better packing achieved with the long-chain methyl-terminated SAM that partially blocks the CdS SILAR. Importantly, the data also suggest that for SAMs with similar size (APPA, BPA, and PPA), the identity of the tailgroup does not affect the amount of CdS uptake on the SAM-coated TiO_2 surfaces.

CdS QDs on Planar Surfaces. Figure 4a shows the UV−vis absorption spectra of the APPA-coated planar TiO_2 surfaces (~2 nm TiO_2 deposited by ALD on quartz microscope slide substrates) after varying numbers of SILAR cycles. First, as expected, the increase in the

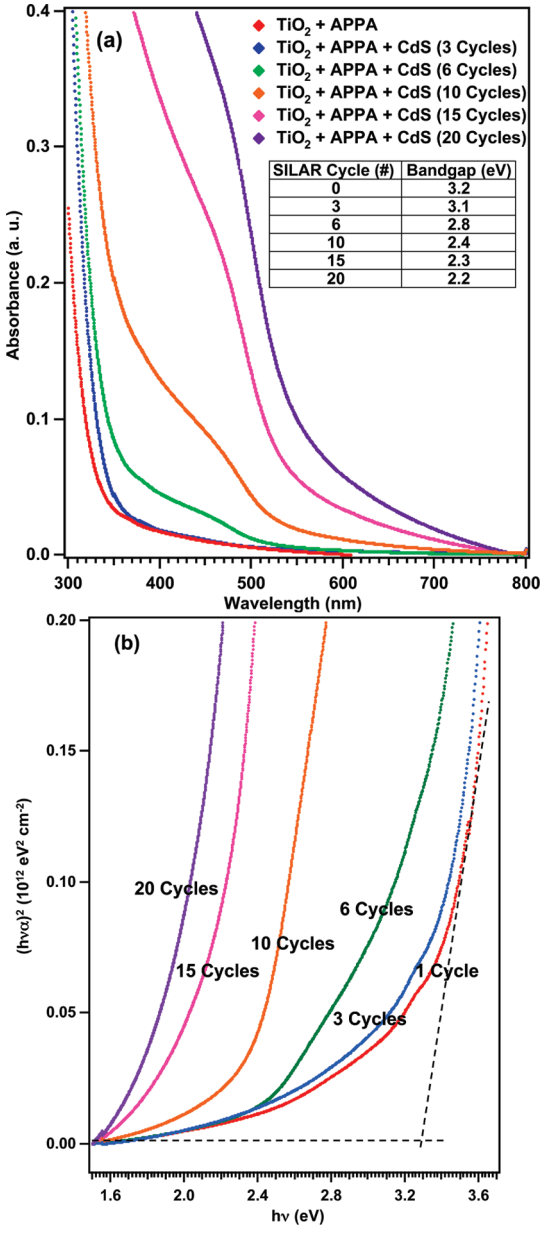

Figure 4. (a) UV−visible spectra and (b) Tauc plots of APPA-coated planar TiO_2 surface at different number of CdS SILAR cycles. To determine the band gap in the Tauc plots, a tangent is first drawn to the baseline at low energies. Second, a line tangent to the slope in the linear region of the absorption onset is drawn. The intersection of the two lines corresponds to the best estimate for the energy of the band gap (an example of this procedure is shown with the dotted lines for the case of the APPA in panel b). Inset in (a) shows the calculated band gap values at each SILAR cycles.

overall absorbance with successive SILAR cycles represents deposition of higher amounts of CdS. Moreover, we observe that the absorption edge shifts to the red with successive deposition cycles. Such behavior is due to size quantization effects and is consistent with the presence of CdS QDs.[11,27,28] Further analysis, including transmission electron microscopy (TEM), also supports the conclusion that CdS QDs are formed (*vide infra*). The Bohr exciton diameter of CdS is 5.8 nm and the

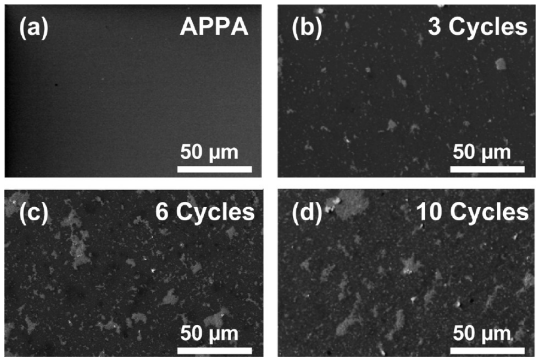

Figure 5. SEM image of planar TiO_2 surface (a) after APPA SAM growth, and after (b) 3 cycles, (c) 6 cycles, and (d) 10 cycles of CdS SILAR.

quantum confinement occurs when the size of the crystallite is comparable to or below 5−6 nm.[29,30] By employing a Tauc analysis of $(\alpha h\nu)^2$ *versus* $h\nu$ plotted in Figure 4b,[31] we extract the band gap values of the CdS nanocrystallites corresponding to each SILAR cycle. The calculated band gaps (Figure 4a inset) vary from 3.2 eV (with no CdS, reflecting the TiO_2 band gap) to 2.4 eV (after 10 CdS SILAR cycles).[28] This indicates that the process reaches the CdS bulk properties after 10 SILAR cycles. By comparing these values with the known values in the literature, the sizes of the CdS QDs are estimated to be ∼2 to ∼6 nm.[28] Interestingly, the calculated band gap values for the 15 and 20 SILAR cycles are 2.2 and 2.3 eV, respectively, which are lower than the band gap of the CdS bulk (2.4 eV). Previous reports have also identified this phenomenon and related it to a high degree of disorder in the CdS as well as a result of non-uniform absorption of UV−vis light of different wavelengths within the thickness of the CdS film.[11]

Figure 5 shows scanning electron microscopy (SEM) images taken from the surface at different SILAR cycles. Interestingly, we detect the presence of large aggregates at the surface even after 3 SILAR cycles. The size of these aggregates increases with more SILAR cycles. Moreover, AES point analysis of the surface indicates that these large aggregates are composed mainly of CdS (>98% with 1−2% CdO). Nevertheless, our UV−vis spectra (Figure 4) suggest that size quantization effects are preserved even after crystallite aggregation. Hence, we conclude that nanoscale CdS particles (QDs) are present within these larger CdS aggregates. The phenomenon in which size quantization is retained even as aggregates form has been previously reported in the literature for SILAR,[11] and it was also observed for other SAMs studied in this work as well as the uncoated surface.

CdS QDs on Nanostructured Surfaces. Similar to the planar surfaces, UV−vis measurements of nanoporous TiO_2 reveal characteristic spectral shifts up to 10 SILAR cycles, indicating the presence of CdS QDs. Figure 6

shows typical UV−vis absorption plots for nanostructured TiO_2/CdS QDs with APPA SAMs as well as for samples that lack any SAM at different levels of CdS SILAR deposition. Similar to the case of planar TiO_2, the Tauc analysis of $(\alpha h\nu)^2$ *versus* $h\nu$ shows that ~2 to ~6 nm CdS QDs are present at the surface and bulk-like CdS properties are observed after 10 SILAR cycles (Tauc plots of APPA-coated nanostructured TiO_2 surface at different number of CdS SILAR cycles are shown in the Supporting Information, Figure S3). Interestingly, investigation of the absolute UV−vis absorbance values in Figure 6 suggests that CdS uptake at nanostructured TiO_2 surfaces is not significantly higher when SAMs are present in nanostructured devices compared to the control samples without a SAM. Also, the band gap values extracted from the Tauc plots, reflecting the size of the quantum dots determined by comparison to the literature,[28] do not change when a SAM is present. Although the data shown are for APPA, we observe similar spectral shifts and absolute UV−vis absorbance values in nanoporous TiO_2 devices with PPA (carboxylic acid-terminated SAM), BPA (short alkyl chain methyl-terminated SAM), and ABPA (aromatic amine-terminated SAM). These results indicate that neither CdS uptake in nanostructured devices nor the size of the CdS QDs are significantly affected by the SAM tailgroup or aromaticity.

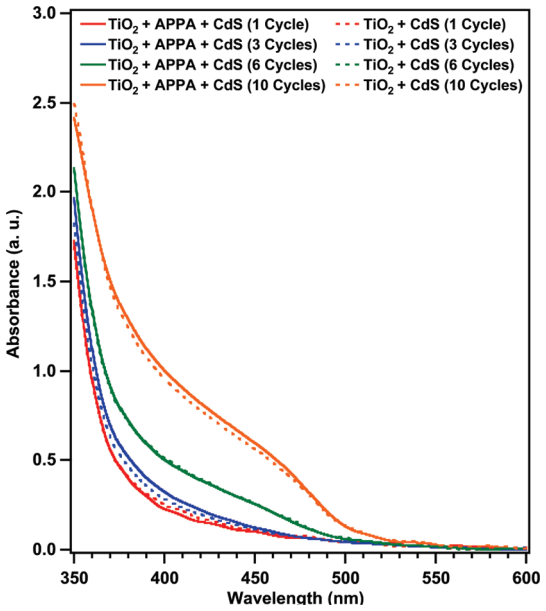

Figure 6. UV−visible spectra of nanostructured TiO_2 surfaces at different numbers of CdS SILAR cycles. Spectra shown here correspond to devices with the APPA SAM as well as devices with no SAM.

Figure 7a−c shows high-resolution TEM images of the APPA-coated nanostructured TiO_2 surface after 6 CdS SILAR cycles. From the lower magnification image of Figure 7a, the presence of nanoparticles can be seen. At higher magnification, the results indicate that there are two types of particles present in these nanostructures, namely, TiO_2 nanoparticles with an average size ranging from 20 to 25 nm (Figure 7b) and CdS nanocrystallites with an average size ranging from ~5 to ~7 nm. These particle sizes are consistent with the size of TiO_2 particles in the commercial paste and with the CdS quantum dot size inferred from UV−vis spectroscopy analysis. In these TEM images, the TiO_2 and CdS lattice fringe spacings can be distinguished at 0.37 and 0.33 nm, respectively, allowing identification of the different particles. These values also suggest that TiO_2 is in the anatase phase[32,33] and CdS is in the cubic(111) phase.[34−36]

The TEM data provide compelling evidence that CdS QDs are present within the TiO_2 nanoporous network. Although aggregates of CdS (as observed by SEM on the planar surfaces) could exhibit quantum confinement effects if they had some features with sizes corresponding to the Bohr radius, it is unlikely that these are the origin of the spectral shifts measured in the UV−vis spectra for two reasons. First, the TEM images clearly show the presence of discrete nanoscale CdS particles with diameters consistent with the QD size predicted by the UV−vis spectra. Moreover, similar size quantization behavior is observed by UV−vis spectroscopy on the planar as on the nanoporous TiO_2 samples where aggregates are unlikely to form since the size of the pores (~20 nm) restricts their growth.

Device Performance. Table 1 shows the dependence of short-circuit current density (J_{sc}), open-circuit voltage (V_{oc}), fill-factor (FF), and power conversion efficiency on number of CdS SILAR cycles for nanostructured TiO_2 devices made by spiro-OMeTAD (2,2',7,7'-tetrakis-(*N*,*N*-di-*p*-methoxyphenylamine)-9,9'-spirobifluorene) spin-coating and top contact (silver)

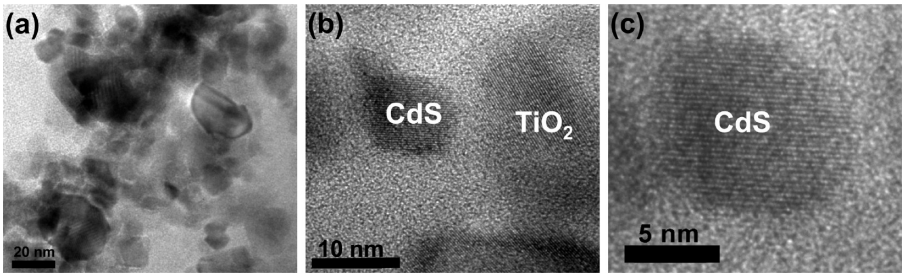

Figure 7. High-resolution TEM images of APPA-coated nanostructured TiO_2 sensitized with CdS nanoparticles after 6 CdS SILAR cycles; scale bars (a) 20 nm, (b) 10 nm, and (c) 5 nm.

TABLE 1. Summarized Data set of J_{sc}, V_{oc}, FF, and Power Conversion Efficiencies for Solid-State CdS QDSSCs with Various SAMs and with No SAM

SAM	SILAR cycle (#)	J_{sc} (mAcm)	V_{oc} (V)	FF	efficiency (%)
APPA	1	0.26	0.59	0.57	0.09
	3	0.49	0.61	0.50	0.15
	6	1.04	0.62	0.67	0.44
	10	0.27	0.70	0.86	0.16
PPA	1	0.21	0.50	0.46	0.06
	3	0.44	0.58	0.63	0.18
	6	1.10	0.60	0.69	0.44
	10	0.20	0.21	0.36	0.02
BPA	1	0.19	0.49	0.62	0.07
	3	0.56	0.52	0.64	0.15
	6	1.07	0.54	0.75	0.43
	10	0.08	0.16	0.29	0.01
ABPA	1	0.23	0.53	0.62	0.05
	3	0.72	0.45	0.57	0.13
	6	0.26	0.26	0.37	0.02
	10	0.12	0.23	0.37	0.01
no SAM	1	0.22	0.54	0.61	0.07
	3	0.32	0.62	0.71	0.14
	6	0.20	0.63	0.57	0.07
	10	0.27	0.70	0.54	0.10

evaporation. Devices with various SAMs (APPA, PPA, BPA, and ABPA) as well as devices with no SAM were measured. SAMs are expected to be stable under the low potentials swept in this measurement as observed elsewhere.[37] Electromigration of the quantum dots during electrical testing is also not expected due to the presence of spiro-OMeTAD in the TiO_2 pores, which should significantly impede any such movement. Figure 8 shows typical current density *versus* voltage (*J*−*V*) curves of devices made with the APPA SAM. Overall, Figure 8 and Table 1 show that the solar cell performance depends upon the number of SILAR cycles employed for deposition of the CdS QDs. We will first discuss this dependence. Next, the electrical performance similarities between devices with different SAMs will be discussed, and then we compare those with the devices made without a SAM.

First, Figure 8 and Table 1 show a general increase in the J_{sc} with increasing SILAR cycles up to a certain SILAR cycle, followed by a consecutive decrease in the J_{sc}. As an example, for the case of APPA, the electrical measurements show that the highest J_{sc} (~1.1 mA/cm^2) and power conversion efficiency (~0.44%) are achieved with 6 SILAR cycles. In these devices, as well as those with PPA and BPA SAMs, the increase in the photocurrent after 6 SILAR cycles likely represents more photon harvesting and possibly lower electron−hole recombination due to larger spatial separation between electron and hole conductors. The decrease in the photocurrent from 6 to 10 SILAR cycles may be related to the aggregation of CdS,[11] the presence of more recombination sites as the CdS bulk-like properties are reached,[18] and possibly lower spiro-OMeTAD pore-filling efficiency due to larger size of the particles.[10] Nevertheless, the highest V_{oc} (~0.70) and FF (0.86) are observed in the case of the APPA SAM and after 10 SILAR cycles.

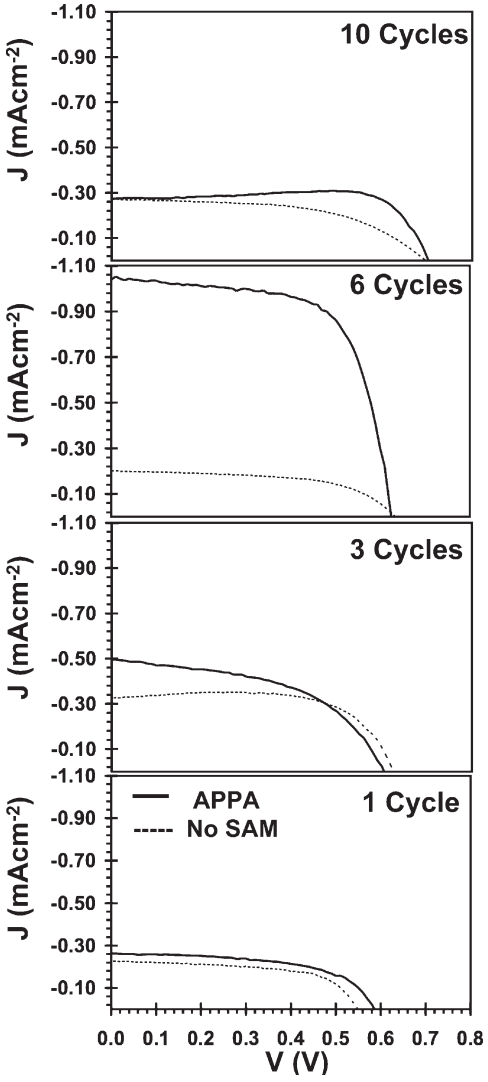

Figure 8. Dependence of current density *vs* voltage curves of the APPA and no-SAM-based solid-state CdS QDSSCs on the number of CdS SILAR cycles.

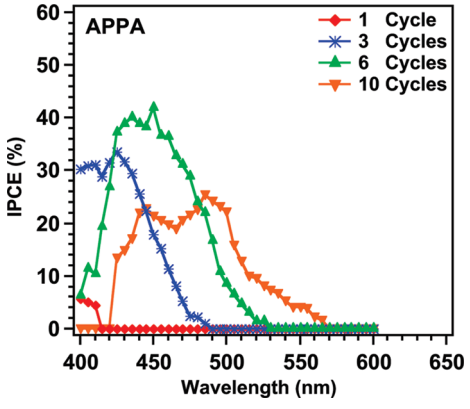

Figure 9. Dependence of IPCE spectra of APPA-based solid-state CdS QDSSCs on the number of CdS SILAR cycles.

Figure 9 shows the dependence of the incident photon to charge carrier generation efficiency (IPCE) spectra of the APPA-based CdS QDSSC devices on the number of SILAR cycles. We observe the maximum IPCE value after the sixth SILAR cycle, which is in agreement with the *J*−*V* measurements (Figure 8). Also, the onset of photocurrent shifts to the red with successive SILAR cycles, which agrees well with the UV−vis measurements (Figure 6). Due to such a shift, we would expect the devices to be able to utilize more of the visible spectrum at the 10th SILAR cycle (Figure 8). However, our data suggest that lower photocurrent efficiency (Figures 8 and 9) ultimately outweighs any benefits achieved from such shifts and thus lower device efficiencies are observed at the 10th SILAR cycle. Moreover, the observation of similar trends in the IPCE and UV−vis spectra confirm that generation of the photocurrent arises mainly from the excitation of the CdS QDs.

Second, we studied the dependence of the device performance on the SAM. Table 1 shows that, in general, similar J_{sc} and device efficiencies are collected for the APPA, PPA, and BPA SAMs. Also, we observe similar IPCE spectra in devices that utilize the PPA SAM (Supporting Information Figure S4) as those that utilize APPA (Figure 9). Hence, these data suggest that the identity of the SAM tailgroup does not significantly affect the device performance.

Moreover, we investigated the effect of aromaticity in devices by employing the ABPA SAM. ABPA and APPA molecules have a similar size and tailgroup (amine termination). However, at any number of SILAR cycles, we observe that the V_{OC} and overall device efficiencies are higher when APPA is employed as the SAM (Table 1). As mentioned previously, we did not observe significantly different CdS uptake between the different SAMs, and hence the origin of better device efficiency for the case of APPA cannot be related to higher content of the sensitizer (CdS). Instead, better device performance may arise from better packing of the APPA compared to ABPA, the presence of fewer recombination sites in the case of the alkyl SAM, and the possibility that charge transfer through the aromatic SAM assists charge recombination. More studies would be required to probe the nature of aromatic SAM packing at these surfaces.

Third and most interestingly, with the exception of the ABPA SAM, we observe up to ∼3 times higher maximum power conversion efficiencies in the devices with a SAM compared to those without a SAM (Table 1 and Figure 8). Further investigation of the data reveals that higher J_{sc} values lead to such dramatic differences. Moreover, at any number of SILAR cycles, we observe lower dark current density when a SAM is present (as an example, the *J*−*V* curves under dark condition and after 3 SILAR cycles are shown in Supporting Information Figure S5). Consequently, we propose that the SAMs may be acting as recombination barriers or passivating defects at the TiO_2 surface, which ultimately results in higher efficiency observed in devices with a SAM. This assertion is supported by the fact that, as shown in Figure 6, we do not see significant improvement in the CdS uptake with SAMs, so the origin of the effect is not merely a higher concentration of quantum dots.

With the data indicating that the SAMs are acting as a recombination barrier or passivating layer, the results obtained in this study lead us to further propose a geometry in which the CdS quantum dots are positioned at the interface between the SAM and the TiO_2. As discussed earlier, no SAM tailgroup dependence is observed in the devices investigated in this work (*i.e.*, similar absolute UV−vis absorbance is measured for different SAMs of the same length, indicating similar CdS uptake). Second, although only probed at the planar TiO_2 surfaces, the data presented in Figure 3 suggest that the CdS uptake is enhanced when SAMs with shorter alkyl chains are utilized, with longer chains partially blocking the CdS SILAR. Third, CdS deposition is observed on the nanostructured TiO_2 surfaces that are passivated by the BPA SAM, even though there are no reactive sites present at such a short-chain methyl-terminated SAM (Figure 6). The absence of a tailgroup dependence, the ability to deposit on nonreactive SAMs, and the preferential adsorption of CdS on shorter tail SAMs all lead us to conclude that CdS QDs are not sitting at the surface of the SAM, but rather have penetrated into the SAM network and reside at the SAM/TiO_2 interface. Such a model is consistent with related studies of inorganic film growth on SAM-terminated surfaces.[38] Although the best power conversion efficiencies reported herein remain less than 1%, which motivates future studies, the results provide important evidence that adding an interfacial SAM in QDSSC devices plays a favorable role in influencing electron transport.

CONCLUSIONS

In summary, we have investigated organophosphonate SAMs as organic linkers in solid-state CdS QDSSCs by various spectroscopic and microscopic techniques as well as electrical measurements. The ∼2 to ∼6 nm QDs were grown by the SILAR method on both planar or nanostructured TiO_2 surfaces. It is found that, with the exception of the long-chain methyl-terminated SAM, slightly higher CdS uptake takes place at the planar TiO_2 surfaces when a SAM is present. However, the nature of the tailgroup does not seem to affect the CdS uptake at either planar or nanostructured TiO_2 surfaces. Overall, maximum power conversion efficiencies can be almost tripled when such SAMs are utilized in solid-state CdS QDDSCs, which may be related to the presence of a recombination barrier or passivation of surface defects. More studies should be carried out to investigate long-term device stability,

optimize QD growth on various SAMs, and to fine-tune pore filling of the QD/SAM-covered nanoporous TiO_2 with spiro-OMeTAD in order to realize superior devices.

METHODS

Materials. Silicon samples were cleaved from 4 in. Czochralski (CZ) grown n-type Si(100) (Silicon Quest) with resistivity ranging from 1.0 to 5.0 Ω·cm and a native silicon oxide layer with thickness of ~17−19 Å. Fluorine-doped SnO_2 (FTO) substrates with a resistivity of ~15 Ω·cm were purchased from Pilkington and used in device fabrication. Quartz microscope slides (Quartz Scientific Inc.) were used as substrates for determination of the band gap using ultraviolet−visible spectroscopy (UV−vis). All reagents were used as purchased, including methanol (EMD Chemicals Inc., ACS grade), ethanol (EMD, ACS grade), chloroform (EMD, ACS grade), acetone (Fisher, ACS grade), hydrogen peroxide (EMD, ACS grade, 30 wt % in H_2O), hydrochloric acid (EMD, ACS grade, 37 wt %), and sulfuric acid (98 wt %, EMD, ACS grade). Aminomethylphosphonic acid (AMPA; 99%, Alfa-Aesar), 3-aminopropylphosphonic acid (APPA; 99%, Aldrich), 4-aminobenzylphosphonic acid (ABPA; 95%, Sigma), 1-butylphosphonic acid (BPA; 98%, Alfa-Aesar), *n*-octadecylphosphonic acid (ODPA; Alfa-Aesar), 3-phosphonopropionic acid (PPA; 94%, Alfa-Aesar), cadmium sulfate ($CdSO_4$; 99.999%; Aldrich), sodium sulfide (Na_2S; >98%, Sigma-Aldrich), and 2,2′,7,7′-tetrakis-(*N*,*N*-di-*p*-methoxyphenylamine)-9,9′-spirobifluorene (spiro-OMeTAD; EMD Chemicals; Merck Gmbh) were used as purchased without further purification.

Substrate Cleaning and TiO_2 ALD. Particles and adventitious organics at the as-received Si surfaces or quartz microscope slides were first removed by 10 min sonication in neat acetone followed by chloroform with deionized water rinses between each solvent bath. The samples were subsequently blown dry with pressurized air. Silicon samples terminated with silicon dioxide were then cleaned for 15 min in a fresh Piranha cleaning solution with 7:3 ratio of 98% sulfuric acid/30% hydrogen peroxide, then rinsed in deionized water, and dried with pressurized air. For planar samples, TiO_2 was deposited on the Piranha-cleaned Si wafer or microscope slide *via* ALD using a 4-in.-wafer-compatible, custom-built ALD reactor previously described.[39] ALD is an important technique for deposition of ultrathin films with excellent conformality and uniformity.[40] TiO_2 ALD films were deposited at 300 °C using titanium tetrachloride ($TiCl_4$) and water (H_2O) as the precursors with 2 s pulse times separated by a 10 s N_2 purge at 20 sccm [sccm denotes cubic centimeter per minute at STP] flow rate. Fifty ALD cycles were employed to grow ~2 nm TiO_2 (measured by ellipsometry) on the substrates. We have found that cleaning the TiO_2 films with methods such as ozone cleaning, O_2 plasma cleaning, and Piranha cleaning generally leads to significant surface roughening, damage, or even total loss of the films. Consequently, the TiO_2 films were only stored in an oven at ~80 °C prior to the SAM growth.[14]

SAM Formation. To form the SAMs, TiO_2 samples were dipped into 10 mM SAM solutions (*vide infra*). Different SAMs with phosphonic acid headgroups and varied chain lengths and tailgroups were attached to the TiO_2 substrates from solution. These SAMs are shown schematically in Figure 1. They can be grouped into three different categories based on the identity of their tailgroup, namely (1) SAMs with an amine tailgroup (AMPA, APPA, and ABPA), (2) SAMs with a methyl tailgroup (BPA and ODPA), and (3) a SAM with a carboxylic acid tailgroup (PPA). We studied the effects of solvent and dip time on the quality of the SAMs. By employing water contact angle measurements, ellipsometry, and infrared (IR) spectroscopy, we found that SAMs with higher packing densities were grown at the TiO_2 surfaces when dip time was increased to ~72 h. Also, we observed better results when SAMs were grown from acidic (pH ~0.5, from concentrated HCl) methanol solution (for APPA, AMPA, PPA, and ABPA) or acidic (pH ~0.5, from concentrated HCl) ethanol (for ODPA and BPA) solution compared to neutral solutions.

CdS SILAR. CdS QDs were grown on the SAM-passivated or nonpassivated TiO_2 surfaces by the SILAR process. To complete a SILAR cycle, these surfaces were first exposed to $CdSO_4$ (0.1 M) solution for 5 min. They were then rinsed with DI water and immersed in a Na_2S (0.1 M) solution for another 5 min followed by another rinsing with DI water.[11] These SILAR cycles were repeated until the desired size of the CdS QDs was achieved.

Device Fabrication. Solar cell devices based on a solid-state electrolyte, namely, spiro-OMeTAD,[10] were fabricated. Details of the device fabrication including FTO substrate etching, cleaning, and patterning as well as the preparation of the nanostructured TiO_2 are provided elsewhere.[10,41−43] We used aerosol spray pyrolysis deposition at 450 °C to coat the FTO samples with ~100 nm thick compact layer of TiO_2. Next, TiO_2 doctor-blading (using diluted 18-NRT TiO_2 paste from Dyesol with average particle size of ~20 nm) was employed, which was followed by a heat treatment and titanium tetrachloride treatment to achieve a ~2 μm nanostructured TiO_2 layer.[41,42] Samples were subsequently dipped in the SAM solution, which was followed by CdS QD SILAR. Next, spiro-OMeTAD pore filling was completed according to the procedure described elsewhere.[10,43] Finally, a 200 nm thick silver (Ag) counter electrode was deposited by thermal evaporation.[43] Devices were subsequently stored inside a desiccator prior to the electrical measurements. QD/SAM substrates were stable over the time frame of device fabrication.

Film Characterization. WCA measurements were employed to determine the packing of the SAMs. A FTA 2000 dynamic contact angle analyzer was used to measure static WCAs. At least five different points on each sample were measured, and an average WCA value corresponding to measurements on several samples is reported. The accuracy of these measurements was ±2°. Film thicknesses (FTs) were measured using a Gaertner L116C single-wavelength ellipsometer. At least six different points were measured on each sample to check the film uniformity, and an average value corresponding to several samples is reported. The accuracy and repeatability of the measurements were ±0.3 and ±0.1 nm, respectively. An SSI S-Probe monochromatized X-ray photoelectron spectrometer system was used in this work. The XP spectra were taken with an Al (Kα) X-ray source (1486.6 eV) in a UHV system with base pressure in the 10^{-9} Torr range. The survey scans were collected using a hemispherical electron energy analyzer at a pass energy (PE) of 156.5 eV with 1 eV resolution. Furthermore, the Cd(3d), S(2s), and Ti(2p) high-resolution scans were collected at a 55.1 PE with 0.1 eV resolution. The X-ray photoelectron spectroscopy data were processed using a Shirley background correction[44] followed by fitting to Voigt profiles. All peaks were adjusted using the bulk C(1s) peak at 284.6 eV to correct the binding energies for the charge shift.[26] A PHI 700 Scanning Auger Nanoprobe was also used in these studies. A 10 keV 10 nA electron beam was employed to achieve 18−20 nm spatial resolution. The survey scans were collected at 1 eV/step resolution, and each spectrum was averaged over 30 scans to obtain satisfactory signal-to-noise ratios. Elemental analysis was carried out using the Multipak software, and the sensitivity of the Auger signals was calibrated relative to the Cu(LMM) signal at 10 keV. Varian's Cary 6000i UV−vis−NIR spectrophotometer was used to determine the band gap values. A FEI XL30 Sirion scanning electron microscope with FEG (field emission gun) source at a 5 kV operating voltage was employed to image the surfaces. The microstructure of TiO_2 nanoparticles with CdS QDs was analyzed by transmission electron microscopy (TEM; 200 kV FEI Tecnai G2 F20 X-TWIN). The specimen of TiO_2 with CdS QDs was dipped in ethanol and sonicated for 15 min to displace TiO_2 nanoparticles from the substrate. After sonication, the ethanol solution was added drop by drop onto a TEM grid by using a pipet. The TEM grid was purchased from Ted Pella Inc. (catalog number 01824G), and it was composed of an ultrathin carbon

coating on a holey carbon film supported by a 300 mesh gold grid. The TEM grid was placed on a filter paper, so the CdS QDs dispersed in ethanol were accumulated on the grid and the ethanol was absorbed into the filter paper. To increase the number of TiO_2 nanoparticles placed on the grid, the pipetting process was performed at least 50 times. The grid was air-dried overnight before TEM analysis.

Electrical Measurements. A 91160 300 W Oriel solar simulator equipped with a 6258 ozone-free xenon arc lamp and an air mass (AM 1.5 G) filter and a Keithley 2400 source meter was employed for the current density−voltage (*J*−*V*) measurements. The lamp was calibrated using a reference NREL calibrated Si photodiode equipped with an IR cutoff filter. The external quantum efficiency (EQE) (also known as IPCE) measurement was taken at short circuit using monochromated white light from a 100 W tungsten lamp, which was focused through a monochromator. The monochromated illumination, chopped at 40 Hz, was superimposed on top of a continuous-wave white light illumination (10% sun) incident on the device. The photocurrent action spectrum of the device was acquired through a lock-in amplifier, and EQE was calculated by comparing the photocurrent action spectrum of the device to that of a NIST traceable calibration photodiode.

Acknowledgment. We would like to thank the Stanford Nanocharacterization Laboratory (SNL) staff and the staff of the Center for Polymer Interfaces and Macromolecular Assemblies (CPIMA) for their support. This publication was based on work supported by the Center for Advanced Molecular Photovoltaics (Award No. KUS-C1-015-21), made by King Abdullah University of Science and Technology (KAUST).

Supporting Information Available: Auger electron spectra of Si/SiO_2 surface after 50 cycles of TiO_2 ALD, APPA SAM growth, 3, 6, and 10 CdS SILAR cycles; transmission infrared spectra for various SAMs formed at the planar TiO_2 surface; Tauc plots of APPA-coated nanostructured TiO_2 surface at different number of CdS SILAR cycles; dependence of IPCE spectra of PPA-based solid-state CdS QDSSCs on number of CdS SILAR cycles; dependence of current density *vs* voltage curves of the APPA and no-SAM-based solid-state CdS QDSSCs after 3 CdS SILAR cycles under dark condition. This material is available free of charge *via* the Internet at http://pubs.acs.org.

REFERENCES AND NOTES

1. Kamat, P. V. Meeting the Clean Energy Demand: Nanostructure Architectures for Solar Energy Conversion. *J. Phys. Chem. C* **2007,** *111*, 2834–2860.
2. Lewis, N. S.; Crabtree, G. W.; Nozik, A. J.; Wasielewski, M. R.; Alivisatos, A. P. Basic Energy Sciences Report on Basic Reserach Needs for Solar Energy Utilization; Washington, DC, 2005.
3. Grätzel, M. Photoelectrochemical Cells. *Nature* **2001,** *414*, 338–344.
4. Grätzel, M. Dye-Sensitized Solar Cells. *J. Photochem. Photobiol.* **2003,** *4*, 145–153.
5. Chen, C.; Wang, M.; Li, J.; Pootrakulchote, N.; Alibabaei, L.; Ngoc-le, C.; Decoppet, J.; Tsai, J.; Grätzel, C.; Wu, C.; Zakeeruddin, S. M.; Grätzel, M. Highly Efficient Light-Harvesting Ruthenium Sensitizer for Thin-Film Dye-Sensitized Solar Cells. *ACS Nano* **2009,** *3*, 3103–3109.
6. Nozik, A. J. Exciton Multiplication and Relaxation Dynamics in Quantum Dots: Applications to Ultrahigh-Efficiency Solar Photon Conversion. *Inorg. Chem.* **2005,** *44*, 6893–6899.
7. Beard, M. C.; Midgett, A. G.; Hanna, M. C.; Luther, J. M.; Hughes, B. K.; Nozik, A. J. Comparing Multiple Exciton Generation in Quantum Dots To Impact Ionization in Bulk Semiconductors: Implications for Enhancement of Solar Energy Conversion. *Nano Lett.* **2010,** *10*, 3019–3027.
8. Kamat, P. V. Quantum Dot Solar Cells. Semiconductor Nanocrystals as Light Harvesters. *J. Phys. Chem. C* **2008,** *112*, 18737–18753.
9. Snaith, H. J.; Schmidt-Mende, L. Advances in Liquid-Electrolyte and Solid-State Dye-Sensitized Solar Cells. *Adv. Mater.* **2007,** *19*, 3187–3200.
10. Ding, I.-K.; Tetreault, N.; Brillet, J.; Hardin, B. E.; Smith, E. H.; Rosenthal, S. J.; Sauvage, F.; Grätzel, M.; McGehee, M. Pore-Filling of Spiro-OMeTAD in Solid-State Dye Sensitized Solar Cells: Quantification, Mechanism, and Consequences for Device Performance. *Adv. Funct. Mater.* **2009,** *19*, 2431–2436.
11. Baker, D. R.; Kamat, P. V. Photosensitization of TiO_2 Nanostructures with CdS Quantum Dots: Particulate *versus* Tubular Support Architectures. *Adv. Funct. Mater.* **2009,** *19*, 805–811.
12. Hodes, G. Comparison of Dye- and Semiconductor-Sensitized Porous Nanocrystalline Liquid Junction Solar Cells. *J. Phys. Chem. C* **2008,** *112*, 17778–17787.
13. Ulman, A. Formation and Structure of Self-Assembled Monolayers. *Chem. Rev.* **1996,** *96*, 1533–1554.
14. Robel, I.; Subramanian, V.; Kuno, M.; Kamat, P. V. Quantum Dot Solar Cells. Harvesting Light Energy with CdSe Nanocrystals Molecularly Linked to Mesoscopic TiO_2 Films. *J. Am. Chem. Soc.* **2006,** *128*, 2385–2393.
15. Pawsey, S.; Yach, K.; Reven, L. Self-Assembly of Carboxyalkylphosphonic Acids on Metal Oxide Powders. *Langmuir* **2002,** *18*, 5205–5212.
16. Folkers, J. P.; Gorman, C. B.; Laibinis, P. E.; Whitesides, G. M.; Nuzzo, R. G. Self-Assembled Monolayers of Long-Chain Hydroxamic Acids on the Native Oxide of Metals. *Langmuir* **1995,** *11*, 813–824.
17. Pathan, H. M.; Lokhande, C. D. Deposition of Metal Chalcogenide Thin Films by Successive Ionic Layer Adsorption and Reaction (SILAR) Method. *Bull. Mater. Sci.* **2004,** *27*, 85–111.
18. Vogel, R.; Pohl, K.; Weller, H. Sensitization of Highly Porous, Polycrystalline TiO_2 Electrodes by Quantum Sized CdS. *Chem. Phys. Lett.* **1990,** *174*, 241–245.
19. Lee, H.; Wang, M.; Chen, P.; Gamelin, D. R.; Zakeeruddin, S. M.; Grätzel, M.; Nazeeruddin, M. K. Efficient CdSe Quantum Dot-Sensitized Solar Cells Prepared by an Improved Successive Ionic Layer Adsorption and Reaction Process. *Nano Lett.* **2009,** *9*, 4221–4227.
20. Bera, M. K.; Mahata, C.; Chakraborty, A. K.; Nandi, S. K.; Tiwari, J. N.; Hung, J.-Y.; Maiti, C. K. TiO_2/GeO_xN_y Stacked Gate Dielectrics for Ge-MOSFETs. *Semicond. Sci. Technol.* **2007,** *22*, 1352–1361.
21. McCurdy, P. R.; Sturgess, L. J.; Kohli, S.; Fisher, E. R. Investigation of the PECVD TiO_2-Si(100) Interface. *Appl. Surf. Sci.* **2004,** *233*, 69–79.
22. Chakraborty, S.; Bera, M. K.; Maiti, C. K.; Bose, P. K. Effects of Annealing on the Electrical Properties of TiO_2 Films Deposited on Ge-Rich SiGe Substrates. *J. Appl. Phys.* **2006,** *100*, 023706.
23. Leprince-Wang, Y. Study of the Initial Stages of TiO_2 Growth on Si Wafers by XPS. *Surf. Coat. Technol.* **2002,** *150*, 257–262.
24. Snyder, R. G.; Strauss, H. L.; Elliger, C. A. C−H Stretching Modes and the Structure of n-Alkyl Chains. 1. Long, Disordered Chains. *J. Phys. Chem.* **1982,** *86*, 5145–5150.
25. Tillman, N.; Ulman, A.; Schildkraut, J. S.; Penner, T. L. Incorporation of Phenoxy Groups in Self-Assembled Monolayers of Trichlorosilane Derivatives—Effects on Film Thickness, Wettability, and Molecular-Orientation. *J. Am. Chem. Soc.* **1988,** *110*, 6136–6144.
26. Moulder, J. F.; Stickle, W. F.; Sobol, P. E.; Bomben, K. D. *Handbook of X-ray Photoelectron Spectroscopy*; Perkin-Elmer Corp. Physical Electronics Division: Eden Prairie, MN, 1992.
27. Weller, H. Colloidal Semiconductor Q-Particles: Chemistry in the Transition Region between Solid State and Molecules. *Angew. Chem., Int. Ed. Engl.* **1993,** *32*, 41–53.
28. Spanhel, L.; Haase, M.; Weller, H.; Henglein, A. Photochemistry of Colloidal Semiconductors. 20. Surface Modification and Stability of Strong Luminescing CdS Particles. *J. Am. Chem. Soc.* **1987,** *109*, 5649–5655.
29. Wang, Y.; Herron, N. Nanometer-Sized Semiconductor Clusters: Materials Synthesis, Quantum Size Effects, and Photophysical Properties. *J. Phys. Chem.* **1991,** *95*, 525–532.
30. Thambidurai, M.; Murugan, N.; Muthukumarasamy, N.; Agilan, S.; Vasantha, S.; Balasundaraprabhu, R. Influence

of the Cd/S Molar Ratio on the Optical and Structural Properties of Nanocrystalline CdS Thin Films. *J. Mater. Sci. Technol.* **2010,** *26*, 193–199.
31. Tauc, J.; Menth, A.; Wood, D. L. Optical and Magnetic Investigations of Localized States in Semiconducting Glasses. *Phys. Rev. Lett.* **1970,** *25*, 749–752.
32. Ardalan, P.; Pickett, E. R.; Harris, J. S., Jr.; Marshall, A. F.; Bent, S. F. Formation of an Oxide-Free Ge/TiO_2 Interface by Atomic Layer Deposition on Brominated Ge. *Appl. Phys. Lett.* **2008,** *92*, 252902.
33. Wu, L.; Yu, J. C.; Fu, X. Characterization and Photocatalytic Mechanism of Nanosized CdS Coupled TiO_2 Nanocrystals under Visible Light Irradiation. *J. Mol. Catal. A: Chem.* **2006,** *244*, 25–32.
34. Sun, W.-T.; Yu, Y.; Pan, H.-Y.; Gao, X.-F.; Chen, Q.; Peng, L.-M. CdS Quantum Dots Sensitized TiO_2 Nanotube-Array Photoelectrodes. *J. Am. Chem. Soc.* **2008,** *130*, 1124–1125.
35. Ma, Y.; Qi, L.; Ma, J.; Cheng, H.; Shen, W. Synthesis of Submicrometer-Sized CdS Hollow Spheres in Aqueous Solutions of a Triblock Copolymer. *Langmuir* **2003,** *19*, 9079–9085.
36. Gao, F.; Lu, Q.; Xie, S.; Zhao, D. A Simple Route for the Synthesis of Multi-Armed CdS Nanorod-Based Materials. *Adv. Mater.* **2002,** *14*, 1537–1540.
37. Appleyard, S.; Day, S.; Pickford, R.; Willis, M. Organic Electroluminescent Devices: Enhanced Carrier Injection Using SAM Derivatized ITO Electrodes. *J. Mater. Chem.* **2000,** *10*, 169–173.
38. Chen, R.; Kim, H.; McIntyre, P. C.; Bent, S. F. Investigation of Self-Assembled Monolayer Resists for Hafnium Dioxide Atomic Layer Deposition. *Chem. Mater.* **2005,** *17*, 536–544.
39. Bakke, J. R.; King, J. S.; Jung, H. J.; Sinclair, R.; Bent, S. F. Atomic Layer Deposition of ZnS *via In Situ* Production of H_2S. *Thin Solid Films* **2010,** *518*, 5400–5408.
40. Ritala, M.; Leskela, M. *Handbook of Thin Film Materials*; Academic Press: San Diego, CA, 2002.
41. Lee, H.; Leventis, H. C.; Moon, S. J.; Chen, P.; Ito, S.; Haque, S. A.; Torres, T.; Nuesch, F.; Geiger, T.; Zakeeruddin, S. M.; *et al.* PbS and CdS Quantum Dot-Sensitized Solid-State Solar Cells: ``Old Concepts, New Results''. *Adv. Funct. Mater.* **2009,** *19*, 2735–2742.
42. Snaith, H. J.; Humphry-Baker, R.; Chen, P.; Cesar, I.; Zakeeruddin, S. M.; Grätzel, M. Charge Collection and Pore Filling in Solid-State Dye-Sensitized Solar Cells. *Nanotechnology* **2008,** *19*, 424003.
43. Ding, I.-K.; Melas-Kyriazi, J.; Cevey-Ha, N.-L.; Chittibabu, K. G.; Zakeeruddin, S. M.; Gratzel, M.; McGehee, M. D. Deposition of Hole-Transport Materials in Solid-State Dye-Sensitized Solar Cells by Doctor-Blading. *Org. Electron.* **2010,** *11*, 1217–1222.
44. Shirley, D. A. High-Resolution Photoemisson Spectrum of the Valence Bands of Gold. *Phys. Rev. B* **1972,** *5*, 4709–4714.